Available online at www.sciencedirect.com
ScienceDirect
Journal of Solid State Chemistry 180 (2007) 824–833
JOURNAL OF SOLID STATE CHEMISTRY
www.elsevier.com/locate/jssc

Phase transitions in *A*-site substituted perovskite compounds: The $(Ca_{1-2x}Na_xLa_x)TiO_3$ $(0 \leqslant x \leqslant 0.5)$ solid solution

Yuan Li[a], Shan Qin[a,*], Friedrich Seifert[b]

[a]*Department of Geology, Peking University, Beijing 100871, China*
[b]*Bayerisches Geoinstitut, Universität Bayreuth, D-95440 Bayreuth, Germany*

Received 19 July 2006; received in revised form 24 November 2006; accepted 3 December 2006
Available online 21 December 2006

Abstract

The $(Ca_{1-2x}Na_xLa_x)TiO_3$ $(0 \leqslant x \leqslant 0.5)$ *A*-site substituted perovskite compounds have been synthesized and characterized by XRD and Raman spectroscopy at room temperature. The XRD powder diffraction study suggests that the end-member $Na_{1/2}La_{1/2}TiO_3$ crystallizes in the tetragonal space group *I*4/*mcm*. The phase transition from *Pbnm* to *I*4/*mcm* is located between $x = 0.34$ and 0.39 and is driven by the variation of ionic radii at the *A*-site. The observed Raman modes are in agreement with group theory analysis, and the relationships between the behavior of structural parameters (e.g. Ti–O–Ti bond angle), indicated by long-range order, and the corresponding Raman frequency shifts and intensity evolution, indicated by short-range order, are established and discussed in terms of the radius effect and the mass effect.

Keywords: *A*-site substituted perovskite; Rietveld refinement; Raman spectroscopy; Phase transition; $CaTiO_3$; $Na_{1/2}La_{1/2}TiO_3$

1. Introduction

The family of ABO_3-type titanates includes a large number of compounds in which the *A*-site may accommodate alkali, alkaline-earth and rare-earth cations, ranging in valence from monovalent to trivalent. Compositional variations of these perovskite compounds are important in material sciences for their electric and catalytic properties and in earth sciences as indicators of geochemical evolution in geological systems [1,2].

Among naturally occurring perovskite-type titanate compounds, the compositional variations may be represented in the quaternary system $SrTiO_3$–$CaTiO_3$–$Na_{1/2}Ln_{1/2}TiO_3$ (Ln = La, Ce, Nd, Pr)–$NaNbO_3$, and the available data show that the binary series $CaTiO_3$–$Na_{1/2}La_{1/2}TiO_3$ is incomplete in the range 30–40 mol% $CaTiO_3$ [3]. The lack of $Na_{1/2}La_{1/2}TiO_3$-rich compositions in the natural samples is probably due to the lack of suitable rock chemistries and does not necessarily indicate instability of such phases.

In the laboratory, there have been a number of studies on the synthesis and structure of solid solution series involving perovskite end-members. Most of them can be formed and compounded by altering the *B*-site composition; however, there are only a handful of cases of compound formation resulting from the substitution at the *A*-site [4]. The solid solution $Ca_{1-2x}Na_xLa_xTiO_3$ (CNLT) $(0 \leqslant x \leqslant 0.5)$ is a typical *A*-site substituted perovskite between perovskite $CaTiO_3$ and loparite $Na_{1/2}La_{1/2}TiO_3$, which has not been systematically synthesized previously yet to our knowledge. However, the synthetic end-member $Na_{1/2}La_{1/2}TiO_3$ has been described structurally in a number of studies. In most of these works, the perovskite-type $Na_{1/2}La_{1/2}TiO_3$ was claimed to have the undistorted cubic structure with the space group $Pm\bar{3}m$, and La^{3+} and Na^{+} ions are randomly distributed at the 12-fold cuboctahedral site [5–9]. In contrast, some studies showed that $Na_{1/2}La_{1/2}TiO_3$ may crystallize with either orthorhombic (*Pnma*) [1,10] or rhombohedral ($R\bar{3}c$) symmetry [3,11]. These differences might be due to the different synthesis routes and/or slight variations in the Na/La ratio [3].

*Corresponding author. Fax: +86 10 62751159.
E-mail address: sqin@pku.edu.cn (S. Qin).

0022-4596/$ - see front matter © 2006 Elsevier Inc. All rights reserved.
doi:10.1016/j.jssc.2006.12.012

The other end-member in the CNLT series, $CaTiO_3$, has been studied extensively in the past [12–15]. At room temperature, $CaTiO_3$ exhibits the orthorhombic space group *Pbnm* [13,14], the unconventional setting of *Pnma*. This structure could be derived from the $Pm\bar{3}m$ aristotype by octahedral tilting about three four-fold axes of the cubic subcell, and in Glazer's notation [16] the octahedral tilting exhibited by $CaTiO_3$ is written as $a^-a^-c^+$.

In this study, we synthesized the CNLT solid solution by solid-state reaction. By X-ray powder diffraction we analyzed structures of the intermediate members in the series, with particular emphasis on the phase transition and the structural characteristics of the end-member $Na_{1/2}La_{1/2}TiO_3$ ($x = 0.5$). In addition, we present a systematic analysis of unpolarized Raman spectra and discuss the relationship between structural distortion parameters and the Raman frequency shifts by comparing the experimental Raman data with the predicted allowed zero-wave-vector ($q \approx 0$) phonon modes. The purpose of this study is, therefore, to obtain more insight into the structures and to illustrate the influence of the *A*-site substitution on the phase transition.

2. Experimental

Powder samples corresponding to the series $Ca_{1-2x}Na_xLa_xTiO_3$ with nominal compositions $x \sim 0$ to 0.5 in 0.05 intervals were synthesized. The reagents were dried for 5 hours at 1000 °C for TiO_2 (Aldrich 99.99%), 500 °C for $CaCO_3$ (Chempur 99.9%) and La_2O_3 (Heraeus 99.9%) and 150 °C for Na_2CO_3 (Chempur 99.9%). Mixtures of stoichiometric amounts with the addition of 2 wt% excess Na_2CO_3 (to compensate for the sodium vaporized at high temperature) were heated from 500 to 800 °C at a rate of 30 °C per hour. After grinding in an agate mortar, the samples were fired in air at 1050 °C for at least 72 h with periodic regrindings, finally rapidly cooled in air to room temperature. These samples were then analyzed with a JEOL JXA-8100 electron microprobe (EMP) operating at an accelerating voltage of 15 kV and using a beam current of 10 nA with the diameter of 1 μm. A range of standard minerals from SPI was used for standardization and all data were reduced using the PHZ correction routine. The microprobe analysis showed the materials to be close to nominal composition with a systematic Na deficit on the order of 1% and homogeneous at the 2% level. Columns "Nominal *x*" and "Real *x*" in Table 1 demonstrate this agreement.

The room temperature powder X-ray diffraction (XRD) study of the synthesis products was carried out on a Siemens D-5000 diffractometer with Cu$K\alpha_{1,2}$ radiation. Data were recorded between 20° and 130° 2θ with steps of 0.02° and counting time of 10 s per step. Silicon was applied as an internal standard. XRD data were then analyzed using the Rietveld method with the GSAS software [17]. In the refinements, the two wavelengths and an intensity ratio of 2:1 were used. Refined parameters were background coefficients, histogram scale factors, lattice parameters, linewidths, phase fractions and atomic positions.

A RENISHAW Ramanscope System 2000 spectrometer was used for Raman measurements. This system comprises an integral Raman microscope, and the excitation wavelength used was 514.5 nm argon ion laser source. Power of 2 mW was incident on the samples in a 2 μm diameter spot through a standard ×50 Leica microscope objective lens, and a ×10 objective to collect the backscattered radiation with an 1800 grooves per mm^2 grating. The spectra were collected with a 10 s data point acquisition time, a spectra range of 10–1800 cm^{-1} and a spectral resolution around 2 cm^{-1}. All the Raman spectra were recorded at room temperature in a backscattering geometry.

2.1. XRD data and analysis

Complete solubility was observed between the end-members of the series $Ca_{1-2x}Na_xLa_xTiO_3$. The XRD

Table 1
Microprobe analysis, cell parameters and space groups of $Ca_{1-2x}Na_xLa_xTiO_3$ ($0 \leqslant x \leqslant 0.5$) perovskites

Nominal *x*	Real *x**	Cell parameters			*V* (Å^3)	Space group
		a (Å)	*b* (Å)	*c* (Å)		
0.00	0.00(0)	5.3798(1)	5.4421(1)	7.6404(1)	223.69(1)	*Pbnm*
0.05	0.05(2)	5.3835(2)	5.4423(2)	7.6464(3)	224.03(1)	*Pbnm*
0.10	0.11(1)	5.3951(3)	5.4483(3)	7.6596(4)	225.15(2)	*Pbnm*
0.15	0.15(5)	5.4088(3)	5.4522(3)	7.6728(5)	226.27(3)	*Pbnm*
0.20	0.18(6)	5.4222(3)	5.4500(3)	7.6842(5)	227.08(2)	*Pbnm*
0.25	0.25(5)	5.4302(4)	5.4580(3)	7.6926(5)	227.99(2)	*Pbnm*
0.30	0.30(2)	5.4464(4)	5.4606(3)	7.7098(6)	229.29(2)	*Pbnm*
0.35	0.34(0)	5.4554(6)	5.4607(4)	7.7146(9)	229.82(2)	*Pbnm*
0.40	0.39(6)	5.4621(2)	5.4621(2)	7.7333(4)	230.72(2)	*I4/mcm*
0.45	0.45(5)	5.4673(1)	5.4673(1)	7.7475(3)	231.59(2)	*I4/mcm*
0.50	0.50(0)	5.4769(1)	5.4769(1)	7.7539(1)	232.59(1)	*I4/mcm*

Note. * calculated from (Na + La)/2(Ca + Na + La).
The numbers in parentheses are the estimated standard deviations in units of the last digit, those for the cell parameters as given by the GSAS algorithm.

patterns of all samples ($x = 0-0.5$) show mainly diffraction lines of the perovskite-type phases. Two weak diffraction peaks corresponding to unreacted La_2O_3 are present in some XRD patterns, but their relative intensities do not exceed 1.5% of the strongest perovskite peak 112_{Pbnm}. The XRD patterns did not give any indications for (Na,La) ordering at the *A* sites, such as doubling of lattice constants.

In ABO_3-type perovskites, structural distortions from the ideal $Pm\bar{3}m$ aristotype can be described in terms of tilting of rigid BO_6 octahedra. The orthorhombic *Pbnm* and tetragonal *I*4/*mcm* structures could be represented as $a^-a^-c^+$ and $a^0a^0c^-$, respectively, in Glazer's notation [16,18]. The transition from *Pbnm* to *I*4/*mcm* involves the disappearance of two of the three octahedral rotations. The tilts break the $Pm\bar{3}m$ symmetry and produce a series of weak superlattice reflections in the diffraction pattern that are diagnostic of the space group of the phase [19].

Fig. 1 displays the room temperature XRD patterns between 36° and 42° 2θ of the phases in the $Ca_{1-2x}Na_xLa_xTiO_3$ series. At $0 \leqslant x \leqslant 0.34$, the peak splitting is similar to that observed in the XRD pattern of $CaTiO_3$. For the *Pbnm* structure, three groups of peaks appear in this 2θ range, i.e. $(120, 210)_{Pbnm}$ at around 37°, $(121, 103, 211)_{Pbnm}$ at 39° and $(022, 202)_{Pbnm}$ at 41°2θ (Fig. 1). As a function of composition, all the peaks shift toward lower 2θ and the relative intensities of some of the peaks decrease gradually, even peaks disappear. With increasing *x*, the two lines of the doublet $(120, 210)_{Pbnm}$ merge into a single peak and then disappear until $x = 0.34$. The triplet $(121, 103, 211)_{Pbnm}$ also merges into one peak with higher *x*, which persists to the composition $x = 0.5$. The splitting of 0 2 2 and 2 0 2 reflections of the orthorhombic *Pbnm* phase is clear at lower *x*; however, at about $x = 0.34$, only one peak could be identified with the consideration of the Cu*K*α_2 contribution to the XRD profile. From the superlattice reflections and peaks merging, it is proposed that the structures of $Ca_{1-2x}Na_xLa_xTiO_3$ are orthorhombic *Pbnm* in the compositional range of $0 \leqslant x \leqslant 0.34$, isostructural with the end-member $CaTiO_3$.

At $x \geqslant 0.39$, the merged single peak $(120, 210)_{Pbnm}$ is absent or too weak to detect, and the triplet $(121, 103, 211)_{Pbnm}$ and another doublet $(022, 202)_{Pbnm}$ merge into one peak, respectively, which indicates that the structures have transformed to a higher symmetry polymorph with characteristics of tetragonal *I*4/*mcm* structure. In other words, the $(120, 210)_{Pbnm}$ reflections disappear, and the splitting of $(121, 103, 211)_{Pbnm}$ and $(022, 202)_{Pbnm}$ reflections merge into $211_{I4/mcm}$ and $202_{I4/mcm}$, respectively, with the significant amount of Na^+ and La^{3+} into *A*-site in the compositional range of $0.39 \leqslant x \leqslant 0.5$. On the other hand, the structures in this range are not yet cubic, as indicated by the presence of the $211_{I4/mcm}$ peak near 29° 2θ, which will vanish when transforming to $Pm\bar{3}m$.

The refinements of the diffraction data also support the above conclusion drawn from the XRD patterns. The cell parameters obtained from the refinements of the entire

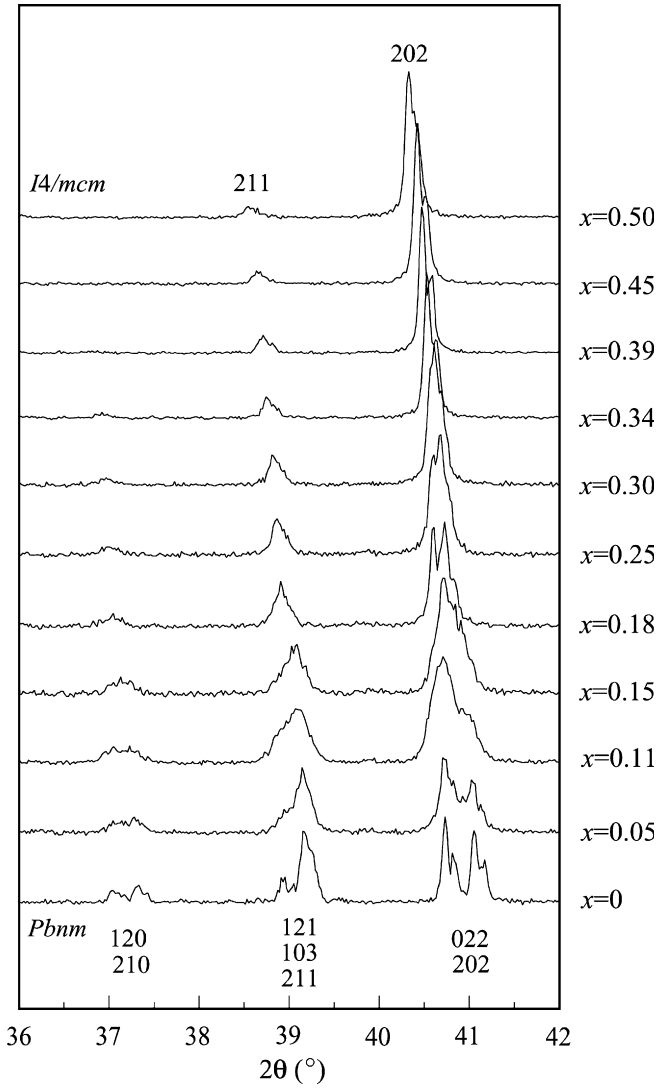

Fig. 1. Portion of XRD patterns of $Ca_{1-2x}Na_xLa_xTiO_3$ ($0 \leqslant x \leqslant 0.5$), showing the compositional dependence of the superlattice reflections. The diffraction lines labeled in the figure are indexed with the orthorhombic *Pbnm* structure (bottom) and tetragonal *I*4/*mcm* structure (top), respectively.

solid solution are listed in Table 1, and the lattice parameters (reduced to those of a pseudocubic subcell) are plotted in Fig. 2. In the compositional range of $0 \leqslant x \leqslant 0.34$, the starting parameters for the Rietveld refinements are taken from our previously published results in the system $CaTiO_3$–$SrTiO_3$ [20], where the procedures of sample synthesis and refinement are very similar to those in this study. From Table 1 and Fig. 2, it is seen that the cell edge lengths of *a* and *b* of the *Pbnm* phase converge near $x = 0.34$ with increasing *x*, indicating a transition to the tetragonal *I*4/*mcm* phase. In the meantime, the volume gradually increases through the entire compositional range. Therefore, we locate the boundary of the phase transition from *Pbnm* to *I*4/*mcm* between $x = 0.34$ and 0.39. However, the refinements in a two-phase mode from $x = 0.35$ to 0.45, give no clues for the co-existence of the two phases. In the view of octahedral tilting [16], the *Pbnm* to

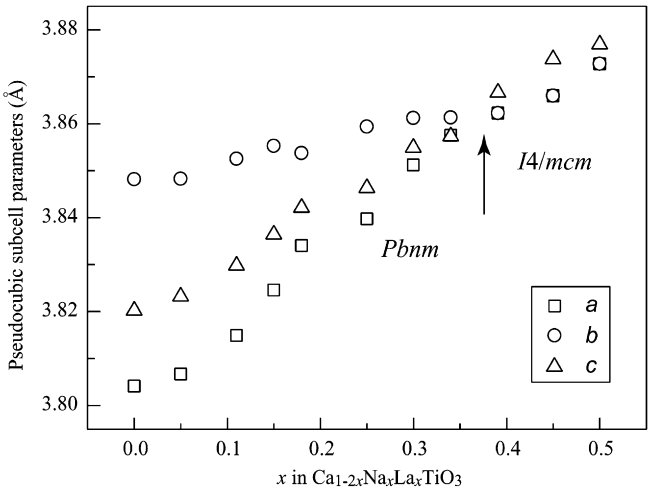

Fig. 2. Pseudocubic subcell parameters plotted as a function of x in $Ca_{1-2x}Na_xLa_xTiO_3$ series. $a = a_0/\sqrt{2}$, $b = b_0/\sqrt{2}$ and $c = c_0/2$ where a_0, b_0 and c_0 are the lattice parameters of the orthorhombic *Pbnm* and tetragonal *I*4/*mcm* unit cells, respectively.

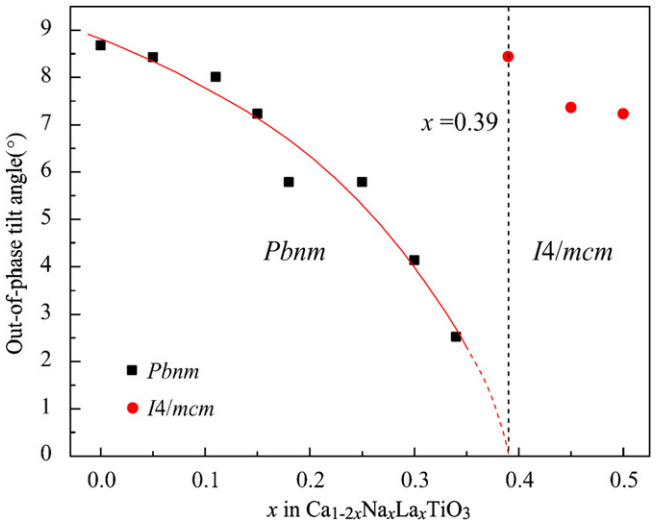

Fig. 3. The out-of-phase octahedral tilt angles as a function of x in $Ca_{1-2x}Na_xLa_xTiO_3$ series. Note that the tilt angles for *Pbnm* were estimated from the lattice parameters, while for *I*4/*mcm* from the internal coordinates.

*I*4/*mcm* transition in perovskites could be represented as $a^-a^-c^+$ to $a^0a^0c^-$, that means the out-of-phase tilts in *Pbnm* will disappear when transferring to *I*4/*mcm*.

It is possible that the intermediate *Imma* phase occurs in the *Pbnm* to *I*4/*mcm* transition [19], as experimentally observed in $SrZrO_3$–$BaZrO_3$ series [21] and $SrZrO_3$ on heating [22,23]. For our present data, however, there is no evidence to figure out the *Imma* phase, possibly due to the limited data quality or the *Imma* phase existing over a very narrow composition range.

Fig. 3 displays the octahedral tilts, extracted from the lattice constants and the internal coordinates, as a function composition x, the extrapolation (the intercept with composition x) of the out-of-phase tilts, corresponding to the *M*-point $(120, 210)_{Pbnm}$ reflections, shows clearly that the boundary from *Pbnm* to *I*4/*mcm* is near $x \sim 0.39$, in agreement with the cell length evaluation. Here the out-of-phase tilts about the diad axis for *Pbnm* structures were calculated by the equation $\theta = \cos^{-1}(a/b)$, while the in-phase tilts for *I*4/*mcm* were estimated from the atomic position of the anion O2 on the 8*h*-site at $(1/4+u, 3/4+u, 0)$ as $\phi = \tan^{-1}(4u)$ [24]. The *Pbnm* in-phase tilts were also calculated, showing that the in-phase tilts will vanish at $x \sim 0.35$, however, the same tendency, comparison with the out-of-phase tilts as a function of x, was observed.

For the end-member $Na_{1/2}La_{1/2}TiO_3$ rhombohedral ($R\bar{3}c$) symmetry has been reported [3,11], which means that in the CNLT series the transition may occur from *Pbnm* to $R\bar{3}c$ ($a^-a^-c^-$) or from *Pbnm* to *I*4/*mcm* to $R\bar{3}c$ [3]. Therefore, we refined the structures in the compositional range $0.39 \leqslant x \leqslant 0.5$ with both tetragonal *I*4/*mcm* and rhombohedral $R\bar{3}c$ structural models. We found that the Rietveld profile refinement using an *I*4/*mcm* model gave a better fit than a refinement with the $R\bar{3}c$ model. In the refinement of $Na_{1/2}La_{1/2}TiO_3$ ($x = 0.5$), for example, the obtained χ^2 value (~2.4) on the basis of *I*4/*mcm* structure is

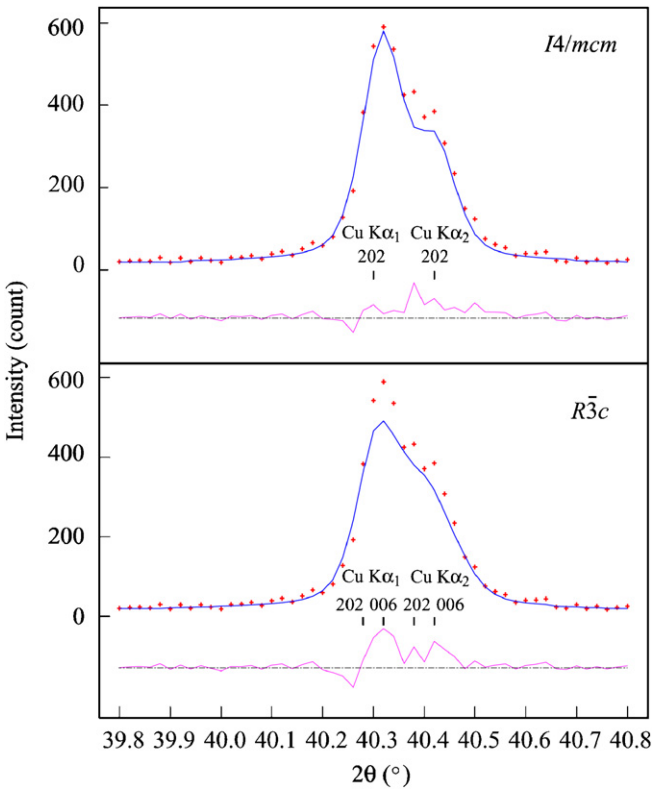

Fig. 4. Observed XRD ($\lambda_{Cu\ K\alpha1} = 1.5405$ Å, $\lambda_{Cu\ K\alpha2} = 1.5443$ Å) pattern (crosses) of $Na_{1/2}La_{1/2}TiO_3$ between 39.8° and 40.8° compared to calculated peak positions (tick marks), fits (upper solid lines), difference curves (lower solid lines) and indices for space groups *I*4/*mcm* and $R\bar{3}c$.

distinctly lower than the χ^2 value (~3.4) based on the $R\bar{3}c$ model. Furthermore, the calculation of diffraction lines and fits for both models compared with the experimental data confirms that *I*4/*mcm*, not $R\bar{3}c$, is the correct space group. Fig. 4 gives such an accurate Rietveld calculation

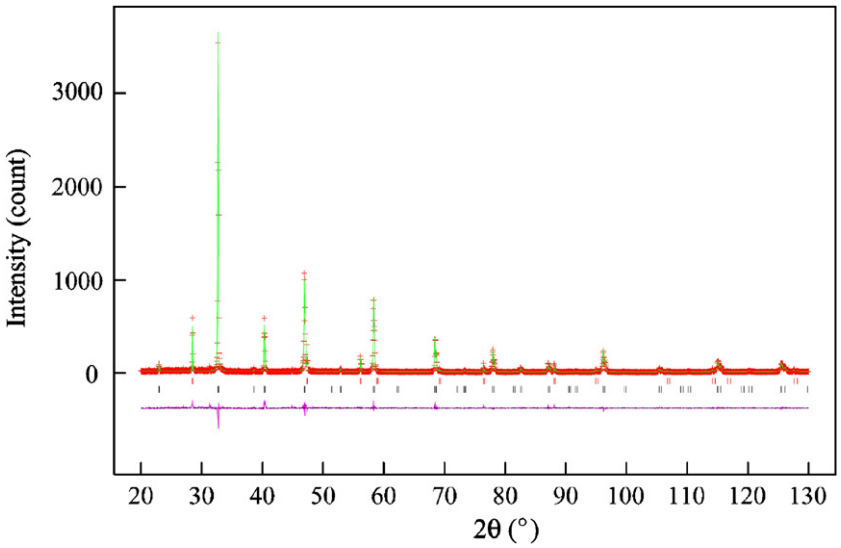

Fig. 5. X-ray diffraction data and calculated pattern for $Na_{1/2}La_{1/2}TiO_3$, the end-member of the $Ca_{1-2x}Na_xLa_xTiO_3$ ($x = 0.5$). The experimental data are shown as crosses, the calculated fits and difference curves as solid lines. Tick marks (upper row for internal standard silicon) indicate the calculated positions of peaks.

Table 2
Crystallographic characteristics for $Na_{1/2}La_{1/2}TiO_3$, the end-member of $Ca_{1-2x}Na_xLa_xTiO_3$ perovskites ($x = 0.5$)

Atom	Position	Atomic positions			B (Å^2)
		x	y	z	
La	4*b*	0	0.5	0.25	0.75(3)
Na	4*b*	0	0.5	0.25	0.75(3)
Ti	4*c*	0	0	0	0.58(4)
O1	4*a*	0	0	0.25	2.4(8)
O2	8*h*	0.2818(15)	0.7818(15)	0	1.2(3)

Note. Finally fitted factors: $R_p = 13.98$, $wR_p = 17.55$, $\chi^2 = 2.404$; space group: $I4/mcm$ (No. 140); cell parameters: $a = b = 5.4769(1)$ Å, $c = 7.7539(1)$ Å.

for $Na_{1/2}La_{1/2}TiO_3$ in a selected 2θ range, where it can be seen that $I4/mcm$ is more appropriate than $R\bar{3}c$. The overall good agreement between the calculated and observed patterns for $Na_{1/2}La_{1/2}TiO_3$ ($x = 0.5$) is illustrated in Fig. 5, and the refined crystallographic data and the agreement factors are given in Table 2.

3. Raman spectra and analysis

Both experimental and theoretical Raman studies for end-member $CaTiO_3$ can be found in the literature [25,26], while neither Raman spectra nor the group theory analysis for the end-member $Na_{1/2}La_{1/2}TiO_3$ have been reported. However, the *A*-site substituted analogies of $Na_{1/2}Bi_{1/2}TiO_3$ ($R3c$) and $K_{1/2}Bi_{1/2}TiO_3$ ($P4bm$) have been analyzed in some qualitative consideration [4,27].

There are a total 24 Raman-active modes for orthorhombic $Pbnm$ ($Z^B = 4$), with four molecular units in the primitive cell, its irreducible representation is $\Gamma_{\text{Raman, }Pbnm} = 7A_g + 5B_{1g} + 7B_{2g} + 5B_{3g}$. While as for tetragonal $I4/mcm$ ($Z^B = 2$), with two molecular units in the primitive cell, gives 7 Raman-active modes, the irreducible representation could be represented as $\Gamma_{\text{Raman, }I4/mcm} = A_{1g} + B_{1g} + 2B_{2g} + 3E_g$. The decrease in the number of phonon modes from 24 to 7 is due to an increase in symmetry, merging non-degenerate $B_{2g} + B_{3g}$ phonons into degenerate E_g and annihilating some A_g.

Fig. 6 displays the unpolarized powder Raman spectra of CNLT samples in the frequency range 10–800 cm^{-1} recorded at room temperature. The bottom curve in Fig. 6 stands for the Raman spectrum for the end-member of orthorhombic $CaTiO_3$ (i.e. $x = 0$), which shows a number of sharp peaks at 154, 181, 225, 246, 286, 335, 470, 494 cm^{-1} respectively (with the letters a–h noted in Fig. 6) and a second broad band at 600–750 cm^{-1}. This is in accordance with the already published data [28–32]. In order to clarify the shifts in a more quantitative way, the observed frequencies of Raman modes and their assignments are given in Table 3. The assignment of these modes is based on the comparison with the analogous behavior of phonon modes in the systems of $CaTiO_3$–$SrTiO_3$ [25,26], $SrTiO_3$–(Ca,Mg)TiO_3 [31], and manganites $RMnO_3$ (R = La, Pr, Nd) [33], as well as first principle calculation [34]. As for the other end-member of tetragonal $Na_{1/2}La_{1/2}TiO_3$ (i.e. $x = 0.5$), the top curve in Fig. 6, most of the sharp peaks in the low-frequency range (10–400 cm^{-1}) disappear compared to the original $CaTiO_3$, and the spectrum shows mainly four bands located near 164, 223, 455 and 528 cm^{-1} superimposed on high backgrounds except for the band at 455 cm^{-1}. In both cases, fewer bands are observed in the Raman spectra than were predicted by the factor group analysis, possibly due to peak overlap or very low polarizability, so as to prevent such bands from being seen in the spectrum.

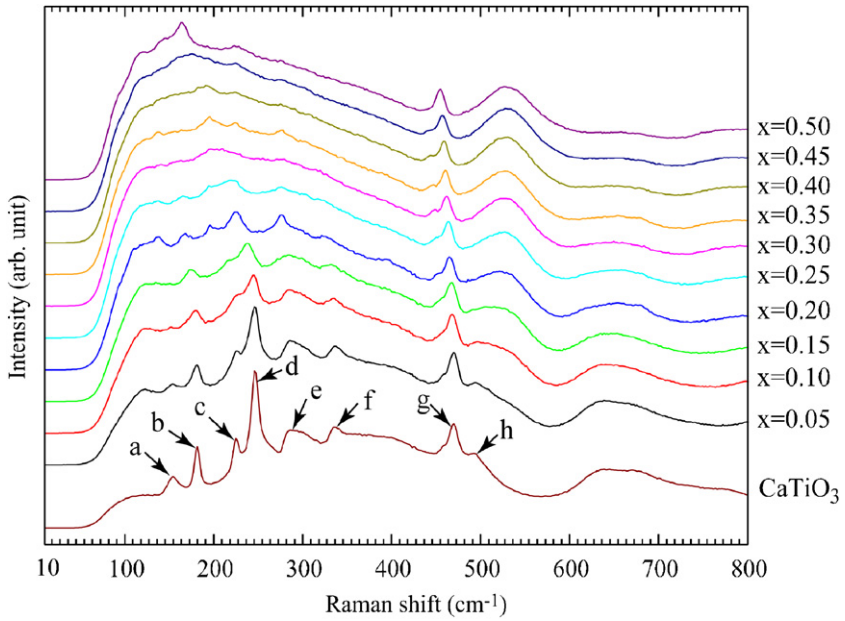

Fig. 6. Unpolarized Raman spectra of perovskite $Ca_{1-2x}Na_xLa_xTiO_3$ ($0 \leqslant x \leqslant 0.5$) at room temperature. The peaks have been labeled with letters from a to h for easy identification when analyzed in the figures and in Table 3.

Table 3
Frequencies (cm^{-1}) of unpolarized Raman bands and their assignments for $CaTiO_3$ perovskite

Band assignment	[28]	[29]	[30]	[31]	[25]	[32]	This work	Labels corresponding to Fig. 6
Ca–TiO_3 lattice mode	155	154	155		153		154	a
O–Ti–O bending modes	180	181	181	175	178	183	181	b
	226	225	226	224	222	227	225	c
	247	246	248	244	244	247	246	d
	286	284	290	286	281	288	286	e
		300	302					
	337	337	340	336	333	339	335	f
Torsional modes	471	469	470	471	467	470	470	g
	495	493	496	492	490	494	494	h

In the CNLT series, three factors related with the structures and phase transition with increasing Na/La content should be considered: ordering–disordering at *A*-site, the mass effect and the radius effect. For ABO_3-type perovskites, the *A*-site substituted solid solution prefers disordering at *A*-site, such as perovskites in the well-studied $Na_{1/2}Bi_{1/2}TiO_3$–$K_{1/2}Bi_{1/2}TiO_3$ or $CaTiO_3$–$SrTiO_3$ systems [4,35]. For the CNLT perovskites, we have seen no ordering evidence in XRD patterns either, probably due to the big difference in scattering factors among the Ca/Na/La cations. It should, however, be noted that for charge compensation some Na–La short-range order might be expected, whereas, for instance, Ca–Sr might be completely random. In Raman spectra, the ordering–disordering scheme is apt to affect the number, width, shape of peaks, rather than the intensity [36]. The broadening and smearing of the Raman features (Fig. 6) should be mainly caused by the largely disordered mixture of dissimilar *A*-cations.

The atomic masses of sodium ($m_{Na} = 22.99$) and lanthanum ($m_{La} = 138.91$) are so different compared with the calcium ($m_{Ca} = 40.08$) that a mass effect should be considered for most of the Raman modes. Generally speaking, the low- and high-frequency ranges are dominated by the vibration of heavy atoms and light atoms, respectively. Owing to replacement Ca^{2+} by La^{3+}/Na^{+}, *A*-site masses gradually increase, the low-frequency bands can be associated with A–O bond, i.e. Na/La–O bond [36]. On the other hand, their ionic radii (12-fold coordination) are different with $r_{Na^+} = 1.39$ Å, $r_{La^{3+}} = 1.36$ Å and $r_{Ca^{2+}} = 1.34$ Å, respectively [37]. The increase of the ionic radii, with *x* increasing, leads naturally to a distortion of the structural framework, the local distortions are expected to impact on the phase transition of $Ca_{1-2x}Na_xLa_xTiO_3$ which can be explained in terms of octahedral tilting, i.e. the lower symmetry structures of *Pbnm* and *I*4/*mcm* can be derived from the prototype $Pm\bar{3}m$. Taking into account the radius effect, the shift and intensity of specific bands in high-frequency range will be expected to be associated with the vibration of distorted octahedra.

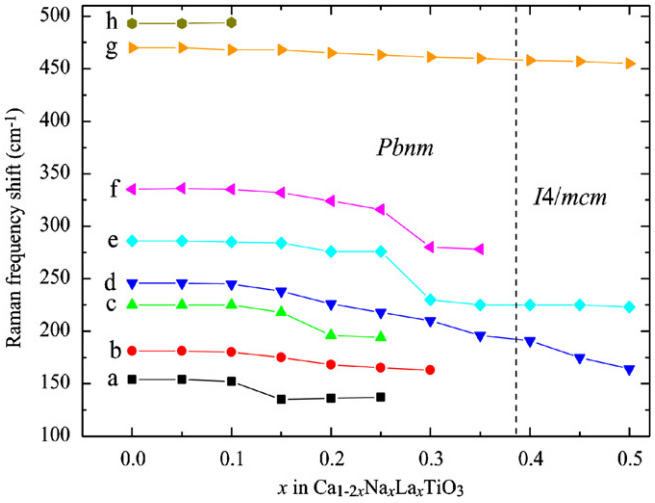

Fig. 7. The evolution of the bands in the whole Raman spectra dependence of composition x at room temperature, the notation (a–h) used throughout this paper for different bands. The phase boundary $x = 0.39$ marked in the figure have been located by XRD analysis.

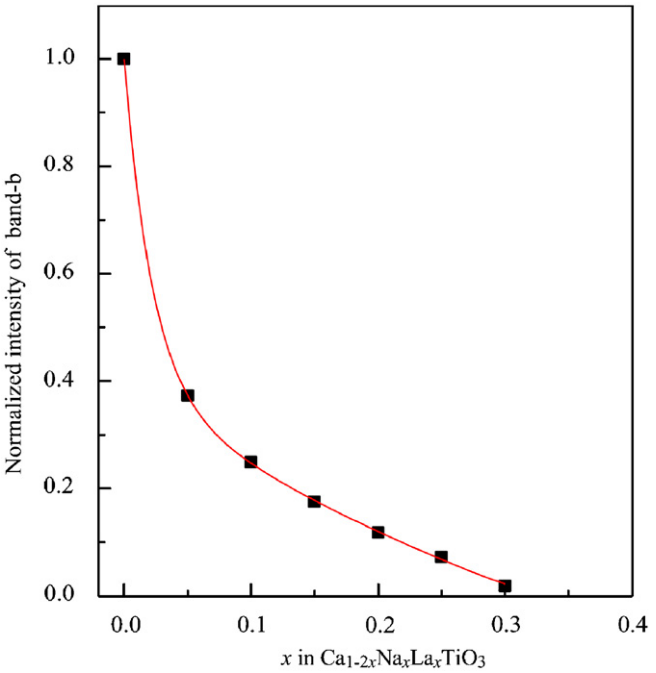

Fig. 8. The relative intensity of band-b as a function of content x, implying that the phase boundary from *Pbnm* to *I4/mcm* is located between $x = 0.35$ and 0.40, in agreement with the XRD result.

Following the evolution of the phonon behavior in the CNLT solid solution, with increasing Na/La content, all the bands observed shift toward lower frequency, broaden and weaken in intensity (Fig. 6). The Raman modes in the low-frequency range have larger frequency shifts than those in high-frequency range, which is similar to the $CaTiO_3$–$SrTiO_3$ system (*Pbnm-I4/mcm–Pm*$\bar{3}$*m*) [25]. Fig. 7 shows the evolution of the frequency shifts with composition x for selected bands. For example, the low-frequency band-d shifts from 246 cm^{-1} ($x = 0$) to 164 cm^{-1} ($x = 0.5$), while the high-frequency band-g at 470 cm^{-1} only decreases to 455 cm^{-1} with the same x variation. In addition, the orthorhombic Raman active modes band-a, band-b, band-c almost disappear simultaneously before $x = 0.35$, while the band-d, band-e and band-g persist until $x = 0.50$, band-f is too weak to be identified above $x = 0.35$.

3.1. Low frequency region, 100–400 cm^{-1}

The 154 cm^{-1} peak (band-a), belonging to the Ca-TiO_3 lattice mode, is a signature of softening, which could be often detected as temperature decrease. But according to first principle analysis, the soft mode in orthorhombic perovskite at low-frequency is not Raman active to first-order scattering, as usual, an observed soft mode probably can be treated as perturbation of the perfect crystal symmetry by grain boundaries or second order processes [34]. The changes of 154 cm^{-1} band observed in CNLT system might be mainly induced by A-site substitution, i.e. with increasing the average A-site mass, the lowest frequency band significantly downshifts until it cannot be detected.

Both the 181 cm^{-1} (band-b) and 225 cm^{-1} (band-c) are associated with the O–Ti–O bending mode. It is known that the location of a phase boundary depends on the degree of lattice distortion of the members in the solid solution, the band-b of A_g symmetry might be diagnostic for the transition from orthorhombic to tetragonal [38]. Fig. 8 presents the intensities of band-b as a function of composition x. Extrapolation shows that the boundary from *Pbnm* to *I4/mcm* is between $x = 0.35$ and 0.40, very close to that obtained from the XRD result.

In the low-frequency range, the best defined and strongest mode is at 246 cm^{-1} (band-d), which keeps shifting to lower frequency until $x = 0.50$, assigned to hard mode B_{1g} and the rotation of oxygen octahedron. Fig. 9 presents the frequency shift of band-d as a function of rotation angle, i.e. Ti–O(2)–Ti bond angle (taken from the refinement of XRD data) for the *Pbnm* phase, and a linear relationship is observed.

The band-e (286 cm^{-1}), band-f (335 cm^{-1}) also shift toward lower frequency with increasing x, which are dominated by Ti–O interior vibrations as a result of tilt of the oxygen octahedron. With increasing La/Na, the band-e keeps downshift all the time, while the band-f is not clear enough to be identified above $x \geqslant 0.40$. The downward shift should be mainly attributed by the increasing average A-cation radius in order to accommodate such cation change, the TiO_6 octahedra will rotate in order to achieve the lowest energy.

3.2. High frequency region, 400–600 cm^{-1}

There is no drastic spectral change like that in the lower frequency. Band-g (470 cm^{-1}), which is related to the A_g mode and described as a TiO_6 distorted octahedron with

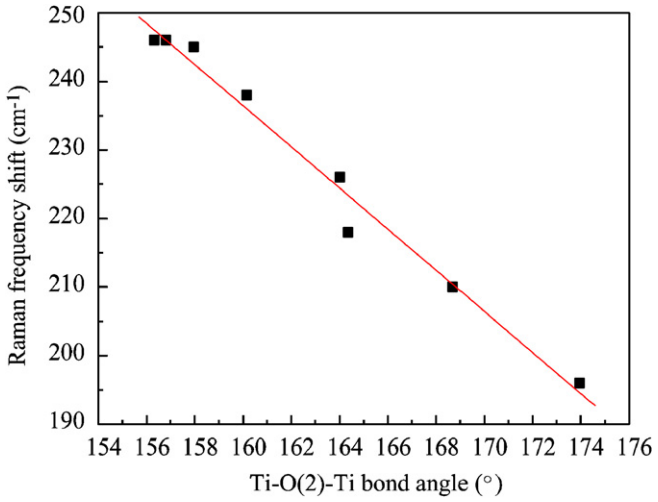

Fig. 9. Raman frequency shift of band-d dependence of the rotation angle, Ti–O(2)–Ti bond angle, for *Pbnm* phase, showing a clearly linear relationship. The line is only guide for the eye.

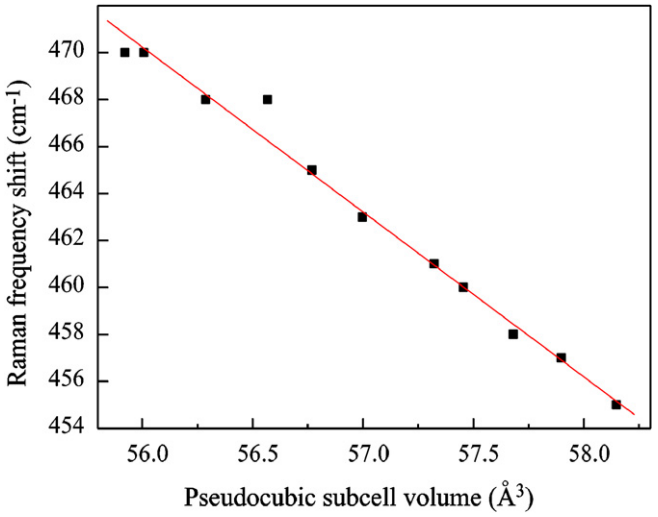

Fig. 10. The Raman frequency shift of torsional mode band-g dependence of pseudocubic subcell volume for $Ca_{1-2x}Na_xLa_xTiO_3$. The line in the figure is only guide for the eye.

large Ti–O–Ti stretching, keeps shifting without peak change until $x = 0.50$. However, the torsional mode of band-h ($497\,cm^{-1}$) disappears when $x \geqslant 0.15$, at the same time one new broad band at around $528\,cm^{-1}$ appears. For oxides, the high frequency Raman bands are dominated by vibration of the TiO_6 octahedra [34]; therefore, this uncommon switch in high-frequency region is expected to be affected by the increasing average ionic radii rather than the mass effect at *A* sites. The extent of distortion can be expressed by the cell volumes, because the cell volumes are related with the average radii at *A* sites. Fig. 10 presents the Raman frequency shift of torsional mode band-g as a function of pseudocubic subcell volume, and a linear relationship is also observed.

4. Discussion and conclusion

The present powder XRD analysis indicates that the sequence of phase transition in the CNLT system, with increasing x at room temperature, is from *Pbnm* ($0 \leqslant x \leqslant 0.34$) to *I*4/*mcm* ($0.39 \leqslant x \leqslant 0.50$). The first-order transition from *Pbnm* directly to *I*4/*mcm* could be seen in some of the other *A*-site substituted solid solution series between ABO_3-type end-members. For example, $Ca_{1-x}Sr_xTiO_3$ in $CaTiO_3$–$SrTiO_3$ system will undergo such a transition between $x = 0.6$ and 0.7 [25,39,40]. In some cases the *Pbnm* to *I*4/*mcm* transition might involve an intermediate phase. The example is $Ba_{1-x}Sr_xZrO_3$, which transforms from *Pbnm* to *I*4/*mcm* with an intermediate orthorhombic *Imma* phase [21]. This sequence of phase transition is also in accord with the behavior of some perovskites on heating, such as the *Pbnm* to *I*4/*mcm* transition at 1373–1423 K [41] or 1500 K [42] for $CaTiO_3$, at 820 K for $SrRuO_3$ [43], or the *Pbnm* to *I*4/*mcm* transition with an intermediate *Imma* phase for $SrZrO_3$ [22,23]. For our data, as discussed in XRD data analysis, it is possible to present an intermediate *Imma* structure, however, it is difficult to locate accurately where the *M*-point reflections disappear due to the weak surperlattice reflections. In other word, the intermediate *Imma* phase is supposed to exist but difficult to detect, maybe it is stable in a narrow x range, or as a coexistence with other phase, the contribution to the diffraction is limited and incomplete for the significant minute amount of intermediate phase.

As mentioned above, the accepted space group for the end-member $Na_{1/2}La_{1/2}TiO_3$ seems to be tetragonal *I*4/*mcm*, not the rhombohedral $R\bar{3}c$ reported by Sun et al. [11] or Mitchell et al. [3]. The difference might be due to the different synthesis routes and/or slight variations in the Na/La ratio. However, in the view of phase transition, the *Pbnm* to *I*4/*mcm* or *Pbnm* to $R\bar{3}c$ corresponds to a discontinuous first-order transition [19]. Although the transition from *Pbnm* directly to $R\bar{3}c$ has been observed in some cases, such as that of the *B*-site substituted perovskites in $LaNiO_3$–$LaFeO_3$ system [44], or that of both the *A*- and *B*-site substituted perovskites in $LaCrO_3$–$SrTiO_3$ series [45], it is scarce in most of the *A*-site substituted perovskites.

In CNLT series, the two different structures observed in the different compositional ranges can be explained in terms of the tolerance factor (t) based on the simple ionic model [46]. For ideal cubic perovskite, the t value should be close to 1, and with the t values slightly less than 1, the structure will lower its symmetry from cubic to tetragonal and finally to orthorhombic. For the t value calculated in $Ca_{1-2x}Na_xLa_xTiO_3$ perovskites, the 12-coordinated effective ionic radii of Ca^{2+} (1.34 Å), Na^+ (1.39 Å) and La^{3+} (1.36 Å) at the *A*-site, the 6-coordinated radius for Ti^{4+} (0.605 Å) and the 2-coordinated radius for O^{2-} (1.35 Å) are taken from Ref. [37], the value *A*–O was obtained using the weighted average of the radii of Ca^{2+}, Na^+ and La^{3+}. A tetragonal symmetry was observed experimentally for

the t values between 0.986 and 0.983, corresponding to $x = 0.5-0.4$; and in the compositional range of $x = 0.34-0$, the lower orthorhombic symmetry is more stable with the t values between 0.982 and 0.973. Thus, the difference in ionic radii at the A-site seems to be the major factor for the *Pbnm* to *I*4/*mcm* transition.

In view of octahedral tilting [16,18], the orthorhombic *Pbnm* has two tilts ($a^-a^-c^+$), an in-phase tilt about the tetrad axis and a tilt about the diad axis of the BO_6 octahedron, which correspond to the M-point and R-point of the cubic Brillouin zone, respectively [24]. The latter is equivalent to two equal out-of-phase tilts about the tetrad axes. In transforming to *I*4/*mcm* ($a^0a^0c^-$), the out-of-phase tilts about the diad axes are removed, and the in-phase tilt about the tetrad axis changes to the out-of-phase tilt. The direct transition from *Pbnm* to *I*4/*mcm* would be first order since this would involve a change in an axis of tilt from the diad to the tetrad axis of the BO_6 octahedron as well as loss of the in-phase rotation.

In conclusion, the present work demonstrates the existence of a complete solid solution series between $CaTiO_3$ and $Na_{1/2}La_{1/2}TiO_3$. The XRD powder diffraction study shows that the perovskite members of the series $Ca_{1-2x}Na_xLa_xTiO_3$ are orthorhombic *Pbnm*, isostructural with orthorhombic $CaTiO_3$, in the compositional range $0 \leqslant x \leqslant 0.34$, and tetragonal *I*4/*mcm* in the range $0.39 \leqslant x \leqslant 0.5$. The phase transition, occurring between $x = 0.34$ and 0.39, is driven by the variation of ionic radii at A-site of the perovskite structures. In contrast to previous studies, the end-member $Na_{1/2}La_{1/2}TiO_3$ is found to be tetragonal *I*4/*mcm*, not cubic $Pm\bar{3}m$, orthorhombic *Pnma* or rhombohedral $R\bar{3}c$. Also, the typical Raman modes and the frequency shifts resulting from the A-site substitution with increasing x are discussed in terms of the radius effect and the mass effect. The relationships between the frequency shifts, intensity evolution and the XRD structural parameters (e.g. Ti–O–Ti bond angle) are characterized, which could potentially give insight into the *Pbnm* to *I*4/*mcm* transition in the $CaTiO_3$–$Na_{1/2}La_{1/2}TiO_3$ series.

Acknowledgments

This work has been supported by the National Natural Science Foundation of China (Grant no. 40672024). The authors thank Dr. Xiang Wu for his help in the Raman spectrum analysis. QS acknowledges DAAD for the financial support in this work. The two anonymous reviewers are also appreciated, their constructive comments are very helpful in improving the manuscript.

References

[1] R.H. Mitchell, in: A.P. Jones, F. Wall, C.T. Williams (Eds.), Rare Earth Minerals: Chemistry, Origin and Ore Deposits, Chapman & Hall, London, 1996, p. 41.
[2] M.A. Pena, J.L.G. Fierro, Chem. Rev. 101 (2001) 1981–2017.
[3] R.H. Mitchell, A.R. Chakhmouradian, P.M. Woodward, Phys. Chem. Miner. 27 (2000) 583–589.
[4] J. Kreisel, A.M. Glazer, G. Jones, P.A. Thomas, L. Abello, G. Lucazeau, J. Phys: Condens. Matter 12 (2000) 3267–3280.
[5] J. Brous, I. Fankuchen, E. Banks, Acta Crystallogr. 6 (1953) 67–70.
[6] A.I. Agranovskaya, Izv. Akad. Nauk. SSSR Ser. Fiz. 24 (1960) 1275–1281.
[7] N.A. Kirsanov, G.V. Bazuev, Zh. Neorg. Chim. 33 (1988) 2909–2912.
[8] Y. Inaguma, J.H. Sohn, I.S. Kim, M. Itoh, J. Phys. Soc. Japan 61 (1992) 3831–3832.
[9] J.P. Miao, L.P. Li, H.J. Liu, D.P. Xu, Z. Lu, Y.B. Song, W.H. Su, Y.G. Zheng, Mater. Lett. 42 (2000) 1–6.
[10] R.H. Mitchell, A.R. Chakhmouradian, J. Solid State Chem. 138 (1998) 307–312.
[11] P.H. Sun, T. Nakamura, Y.J. Shan, Y. Inaguma, M. Itoh, Ferroelectrics 200 (1997) 93–107.
[12] T. Barth, Norsk Geologisk Tidsskrift 8 (1925) 201–216.
[13] S. Sasaki, C.T. Prewitt, D. Bass, W.A. Schulze, Acta Crystallogr. C 43 (1987) 1668–1674.
[14] R.H. Buttner, E.N. Maslen, Acta Crystallogr. B 48 (1992) 644–649.
[15] A. Beran, E. Libowitzky, T. Armbruster, Can. Mineral. 34 (1996) 803–809.
[16] A.M. Glazer, Acta Crystallogr. B 28 (1972) 3384–3391.
[17] A.C. Larson, R.B. Von Dreele (Eds.), GSAS: General Structural Analysis System, LANSCE, Los Alamos National Laboratory, Los Alamos, NM, The Regents of the University of California, 1994.
[18] P.M. Woodward, Acta Crystallogr. B 53 (1997) 32–43.
[19] C.J. Howard, H.T. Stokes, Acta Crystallogr. B 54 (1998) 782–789.
[20] S. Qin, A.I. Becerro, F. Seifert, J. Gottsmann, J. Jiang, J. Mater. Chem. 10 (2000) 1609–1615.
[21] B.J. Kennedy, C.J. Howard, G.J. Thorogood, J.R. Hester, J. Solid State Chem. 161 (2001) 106–112.
[22] C.J. Howard, K.S. Knight, B.J. Kennedy, E.H. Kisi, J. Phys: Condens. Matter 12 (2000) L677–L683.
[23] H. Fujimori, M. Kakihana, K. Ioku, S. Goto, M. Yoshimura, J. Ceram. Soc. Japan 112 (2004) 189–192.
[24] Y. Zhao, D.J. Weidner, J.B. Paise, D.E. Cox, Phys. Earth Planet. Int. 76 (1993) 17–34.
[25] S. Qin, X. Wu, F. Seifert, A.I. Becerro, J. Chem. Soc. Dalton. Trans. 19 (2002) 3751–3755.
[26] S.K. Mishra, R. Ranjan, D. Pandey, P. Ranson, R. Ouillon, J.P. Pinan-Lucarre, P. Pruzan, J. Solid State Chem. 178 (2005) 2846–2857.
[27] J. Kreisel, A.M. Glazer, P. Bouvier, G. Lucazeau, Phys. Rev. B 63 (2001) 174106, 1–10.
[28] U. Balachandran, N.G. Eror, Solid State Commun. 44 (1982) 815–818.
[29] P. McMillan, N. Ross, Phys. Chem. Miner. 16 (1988) 21–28.
[30] P. Gillet, F. Guyot, G.D. Price, B. Tournerie, A.L. Cleach, Phys. Chem. Miner. 20 (1993) 159–170.
[31] T. Hirata, K. Ishioka, M. Kitajima, J. Solid State Chem. 124 (1996) 353–359.
[32] H. Zheng, G.D.C.C. de Györgyfalva, R. Quimby, H. Bagshaw, R. Ubic, I.M. Reaney, J. Yarwood, J. Euro. Ceram. Soc. 23 (2003) 2653–2659.
[33] L. Martin-Carron, A. de Andres, M.J. Martinez-Lope, M.T. Casais, J.A. Alonso, J. Alloy. Compds. 323–324 (2001) 494–497.
[34] V. Zelezny, E. Cockayne, J. Petzelt, M.F. Limonov, D.E. Usvyat, V.V. Lemanov, A.A. Volkov, Phys. Rev. B 66 (2002) 224303.
[35] P. Ranson, R. Ouillon, J.P. Pinan-Lucarre, P. Pruzan, S.K. Mishra, R. Ranjan, D. Pandey, J. Raman Spectrosc. 36 (2005) 898–911.
[36] S. Said, P. Marchet, T. Merle-Mejean, J.P. Mercurio, Mater. Lett. 58 (2004) 1405–1409.
[37] R.D. Shannon, Acta Crystallogr. A 32 (1976) 751–767.
[38] E. Cockayne, B.P. Burton, Phys. Rev. B 62 (2000) 3735–3743.

[39] C.J. Howard, R.L. Withers, B.J. Kennedy, J. Solid State Chem. 160 (2001) 8–12.
[40] H.W. Meyer, M.A. Carpenter, A.I. Becerro, F. Seifert, Am. Mineral. 87 (2002) 1291–1296.
[41] S.A.T. Redfern, J. Phys: Condens. Matter 8 (1996) 8267–8275.
[42] B.J. Kennedy, C.J. Howard, B.C. Chakoumakos, J. Phys: Condens. Matter 11 (1999) 1479–1488.
[43] B.J. Kennedy, B.A. Hunter, Phys. Rev. B 58 (1998) 653–658.
[44] H. Falcon, A.E. Goeta, G. Punte, R.E. Carbonio, J. Solid State Chem. 133 (1997) 379–385.
[45] B.J. Kennedy, C.J. Howard, G.J. Thorogood, M.A.T. Mestre, J.R. Hester, J. Solid State Chem. 155 (2000) 455–457.
[46] V.M. Goldschmidt, Naturwissenschaften 14 (1926) 477–485.